

# Extended Field-Effect Gating of Ionic and Fluidic Transport in Nanopores

*Yang Liu<sup>\*1</sup>, David E. Huber<sup>2</sup>, Vincent Tabard-Cossa<sup>2</sup>, and Robert W. Dutton<sup>1</sup>*

<sup>1</sup>Center for Integrated Systems, Stanford University, CA 94305

<sup>2</sup>Stanford Genome Technology Center, Palo Alto, CA 94304

E-mail: [yangliu@gloworm.stanford.edu](mailto:yangliu@gloworm.stanford.edu), phone: 1-650-723-9796, fax: 1-650-725-7731

**ABSTRACT:** This modeling work investigates the coupled ionic and fluidic transport in field-effect gated nanopores with non-overlapping electrical double layers. We show that such devices exhibit highly nonlinear gating characteristics, which can be significant even in nanopores with radii 50 times the Debye screening length. This is attributed to the extension of the field effect under sufficiently high external electric fields. We interpret such an extended field effect as the suppression of the counter-ion screening in the presence of strong transport processes. Assisted by numerical simulations, the intrinsic correlation between the nonlinear gating characteristics and electro-kinetic phenomena such as concentration polarization and fluid vortex flow is also examined for the gated nanopore devices.

## 1. INTRODUCTION:

Nanopores are emerging as promising platforms for electrically-based bio-sensing applications, including rapid DNA sequencing and single-molecule detection [1,2,3,4,5]. To realize their potential as practical sensors, nanopore devices must be able to effectively manipulate biomolecular transport and control molecule motion during translocation [4]. Electric-field driven actuation is one approach. By analogy with semiconductor field effect transistors (FETs), where electron or hole transport is modulated by manipulating the electrostatics via an adjacent gate electrode [6], microfluidic “transistors” have been created that modulate the magnitude and direction of electroosmotic flow using a buried gate electrode in the channel wall [7]. Similarly, on the nanoscale, field-effect gating has been exploited for ionic [8,9,10,11,12,13] and molecular [8,14] transport in nano-channels or nanopores. A closely related and actively studied area is perm-selective nano-channels [15,16,17,18,19,20,21], which have important applications in sample separation and pre-concentration [16]. In such systems, it has been observed that, inherently coupled ionic and fluidic transport gives rise to a rich collection of correlated effects including concentration polarization (CP), induced electro-osmotic flow (EOF), and nonlinear overlimiting current characteristics [16,17,21]. An improved understanding of the transport effects of field-effect gating in nanopores would greatly facilitate the design of nano-fluidic devices for biomolecule detection and manipulation.

Despite the similarity in the basic concepts of semiconductor and nano-fluidic field-effect devices, their underlying physical mechanisms are fundamentally different. Ionic solutions are essentially zero bandgap conductors with no background doping. This fact results in their lack of depleted space-charge regions, while such regions are central to the operation, particularly the “switch-off”, of semiconductor FETs [6]. In nano-fluidic channels, the field-effect gating always results in the formation of electrical double layers (EDLs), i.e. the accumulation of counter ions, at the gate surface to screen the gating potential [8]. According to the commonly used Guoy-Chapman-Stern (GCS) model for EDLs [22], the extent of the field effect is limited by the Debye screening length,  $\Lambda_D$  ( $\sim 10$  nm and 1 nm respectively for 1 mM and 100 mM ionic strength). This implies that the channel width needs to be comparable in size

to  $\Lambda_D$  for efficient field-effect gating, which would impose stringent constraints on device fabrication and system integration. It should be noted, however, that such a Debye screening behavior is only valid under equilibrium conditions [23,24,25,26,27]. In fact, Onsager et al. [23,24,25] showed that electrolyte screening can be effectively suppressed under a sufficiently high external field. This effect occurs because the “ionic atmosphere” around a charged particle is less developed due to their relative movement and only forms a partial screening layer. It is known to be the basis for the Wien effect when the field strength is comparable to  $k_B T / q \Lambda_D$  [24,26]. Here,  $k_B T / q \sim 26$  mV is the thermal voltage at room temperature. In our previous work, this de-screening effect and the resultant long-range electrostatic interaction were exploited for the detection of the intrinsic charge of biomolecules in nanopore [27] and nanowire [28] sensors. We reason that the same effect also applies to the EDLs formed at the surface of gated nanopores, thereby enabling long-range, electrostatic manipulation of charged species. In a previous simulation study, Daiguji et al. proposed nano-fluidic diodes and bipolar transistors using nano-channels with half channel height  $\leq 5\Lambda_D$  [9], a regime where a small portion of the EDLs still overlap within the channels [16]. In this work, we demonstrate that significant extended field effect exists even in nanopores with radii of  $\sim 50\Lambda_D$ , a regime of fully non-overlapping EDLs.

We numerically study the ionic and fluidic transport in field-effect gated nanopores by self-consistently solving the coupled Poisson-Nernst-Planck (PNP) and Stokes equations. A model device is schematically shown in Fig. 1, where the gate electrode is buried within the solid-state membranes. The devices of particular interest have relatively large radii ( $\sim 50$  nm, corresponding to  $5\Lambda_D$  and  $50\Lambda_D$  at 1 mM and 100 mM ionic strengths, respectively) and short lengths ( $\sim 300$  nm). The modulation characteristics of both ionic and fluidic transport in such devices are analyzed and correlated with electro-kinetic phenomena such as concentration polarization and fluid vortex flow. The observed extended field effect is interpreted as the de-screening of counter-ions in the presence of strong transport processes.

## ***2. TRANSPORT MODEL:***

The device under study (Fig. 1) is a cylindrically symmetric pore connecting two electrolyte reservoirs separated by a solid-state membrane. There are three electrical terminals: the drain, source and gate. The applied bias ( $V_d$ ) between the drain and grounded source electrodes drives the transport. The gate electrode buried inside the oxide dielectrics modulates the transport through gate biasing ( $V_g$ ). We model the nonlinear ionic transport within the pore and reservoirs using the continuum-based Poisson-Nernst-Planck (PNP) equations:

$$\nabla \cdot (\epsilon_w \nabla \psi) + q(C_+ - C_-) = 0,$$

$$\nabla \cdot \vec{J}_+ \equiv q \nabla \cdot (-D_+ \nabla C_+ - \mu_+ C_+ \nabla \psi + C_+ \vec{u}) = 0,$$

$$\nabla \cdot \vec{J}_- \equiv -q \nabla \cdot (-D_- \nabla C_- + \mu_- C_- \nabla \psi + C_- \vec{u}) = 0,$$

where  $\psi$  is the electrostatic potential,  $C_{+/-}$  the cation/anion concentrations,  $\vec{J}_{+/-}$  the cation/anion current densities,  $\epsilon_w$  the solution permittivity,  $\mu_{+/-}$  the cation/anion mobilities,  $D_{+/-}$  the cation/anion diffusion coefficients, and  $\vec{u}$  the solvent velocity. The Einstein relation  $D = \mu k_B T / q$  is used for both ion species. The bulk salt concentration,  $C_0$ , is approached at the top and bottom boundaries. The oxide layers are assumed to be impermeable to ions. Within the oxide layers, we only solve the Poisson equation for electrostatics. Continuity of  $\psi$  is imposed across all the interfaces. For the PNP equations, the Dirichlet boundary condition is used for the salt concentrations at the top and bottom boundaries where the bulk value,  $C_0$ , is approached. The gate electrode region is assumed to be equi-potential,  $\psi = V_g$ . The Dirichlet boundary condition is used for the electrostatic potential at the top ( $\psi = V_d$ ) and bottom ( $\psi = 0$ ) boundaries. The Neumann boundary condition is used at the reservoir side boundaries, where the ionic and electric fluxes are set to zero. The Neumann boundary condition is also applied to enforce zero normal ion flux at the solution/oxide interface.

There are a number of physical effects that we choose to represent implicitly in the ionic transport model. The Stern layer at the solution/oxide interface may contribute an additional dielectric layer with  $\sim 20 \mu\text{F}/\text{cm}^2$  capacitance [29]. We account for this additional capacitance as part of the gate oxide. Also, there is usually a reference energy difference between the solution electrodes (source and drain) and the

metal gate electrode due to affinity differences across the various interfaces [29,30]. We assume such an electrode reference energy offset is already accounted for in the given biases.

The Reynolds number in our nanopore system is low ( $<0.03$ ). Therefore, it is appropriate to model the fluid transport as an incompressible, Newtonian Stokes flow [31], which is governed by the Stokes-divergence equations

$$-\nabla p + \gamma \Delta \vec{u} - q(C_+ - C_-)\nabla \psi - k_B T \nabla(C_+ + C_-) = 0,$$

$$\nabla \cdot \vec{u} = 0,$$

where  $p$  is the solvent pressure and  $\gamma$  the solvent viscosity. Here, the gradient of the excess osmotic pressure from the mobile ions is explicitly treated as a body force (rightmost term), instead of being implicitly included as part of the pressure term. Such a treatment improves the numerical stability since the discretization of the Stokes equations becomes consistent with the Scharfetter-Gummel scheme [32] used for the PNP equations. Boundary conditions for the Stokes equation include [33]: no-slip for the channel surfaces; slip for the symmetry axis; zero pressure and zero normal velocity gradient at the top and bottom reservoir boundaries. For a given set of electrical biases, all of the above transport equations are self-consistently coupled and solved over the entire device structure, which gives the steady-state, terminal I-V characteristics,  $I_d(V_d, V_g)$ . Some physical parameters for the coupled PNP-Stokes simulations include:  $\epsilon_w = 80\epsilon_0$  for water where  $\epsilon_0$  is the vacuum permittivity; symmetric ion mobilities  $\mu_+ = \mu_- = 7.62 \times 10^{-8} \text{ m}^2/\text{Vs}$  for KCl;  $\epsilon_{ox} = 3.9\epsilon_0$  for  $\text{SiO}_2$ ; and  $\gamma = 0.001 \text{ Ns/m}^2$  for water. Validations of the numerical model are given in Fig. S1-S3 of the Supporting Information.

The presence of surface charges at the pore walls can play an important role in the gating process. In practice, the surface charge density can be adjusted as an additional design parameter by either pH control or surface chemistry [34]. To highlight the electrical gating effect, we primarily consider the case of a charge-neutral nanopore surface. We refer the readers to Fig. S5 of the Supporting Information for a brief discussion on the effect of surface charge.

### 3. RESULTS AND DISCUSSIONS

**3.1 Ionic Transport:** The ionic current through the nanopore (i.e. drain current,  $I_d$ ) vs. buried electrode voltage (i.e. gate voltage,  $V_g$ ) characteristics are shown for two distinct nanopore sizes and KCl electrolyte concentrations in Fig. 2. In 1 mM KCl with  $\Lambda_D \sim 10$  nm, the radius of the nominal pore is considerably larger than  $\Lambda_D$  ( $R_0 \sim 5\Lambda_D$ ). The simulated  $I_d$ - $V_g$  curves for this case are given in Fig. 2a. Each  $I_d$ - $V_g$  curve corresponds to a specific drain bias that ranges between 0 V and 3 V. We observe that, under sufficiently high external biases  $V_d$ , the drain current is effectively modulated by the gate biasing  $V_g$ , even though  $\Lambda_D$  is considerably smaller than the pore radius. Each  $I_d$ - $V_g$  curve exhibits a symmetry,  $I_d(V_d, V_g) = I_d(V_d, V_d - V_g)$ . This is expected, considering the symmetric device geometry and equal mobilities for  $K^+$  and  $Cl^-$  ions. The peak current value occurs at the symmetric bias condition,  $V_d = 2V_g$ . This corresponds to the floating gate condition, under which the field-effect gating minimally affects the transport. As the gate bias shifts away from the symmetric condition in either direction, significant drain current suppression is observed. The drain current recovers slightly only at extremely asymmetric conditions.

For comparison, we consider two additional cases, one where the EDLs are fully overlapped and one where the EDL size is further reduced. Figure 2b shows  $I_d$ - $V_g$  curves at 1 mM KCl concentration for a smaller, 5 nm radius nanopore, where the EDLs overlap fully within the pore ( $R_0 \sim \frac{1}{2}\Lambda_D$ ). In contrast to our nominal case, no current peaks are observed near the symmetric bias conditions. Instead, as expected for such nanopores [8], the drain current increases due to enhanced counter-ion accumulation as  $V_g$  shifts toward more asymmetric conditions. For our second case, Figure 2c presents the  $I_d$ - $V_g$  curves for a 50 nm radius pore with 100 mM KCl solution. Here, the increase in electrolyte concentration causes both a decrease in Debye length  $\Lambda_D$  to  $\sim 1$  nm and an increase in ionic current. Remarkably, despite a pore radius corresponding to  $\sim 50\Lambda_D$ , we still observe an appreciable peak in ionic current at symmetric biasing for sufficiently high  $V_d$  values. These results reveal the distinctive difference in the ionic current modulation behavior for devices with overlapping and non-overlapping EDLs.

To characterize the efficiency of the gating process in the non-overlapped pores, we define the modulation depth as the relative difference between the symmetric peak and minimum drain current values,  $\Delta m \equiv (I_{d,sym} - I_{d,min})/I_{d,sym}$ . In general,  $\Delta m$  is determined by a complex interaction of transport processes and is dependent upon such variables as electrolyte concentrations, bias conditions, and both gate and nanopore geometry. The dependence of  $\Delta m$  on the drain bias  $V_d$  is shown in Fig. 2e. For our nominal case with 1 mM KCl,  $\Delta m$  increases monotonically with  $V_d$ 's, reaching ~67% at  $V_d=+3$  V. For the case with 100 mM KCl, the total magnitude of the ionic current is larger but the modulation depth is less significant, reaching a saturation value of ~20% at  $V_d=+1$  V.

To investigate the relative contributions of drift-diffusion and convective transport processes in this extended field-effect gating phenomenon, we examine the ionic transport in the nominal device without the Stokes flow, using only the PNP model (Fig. 2d). In this model, the basic gate modulation is preserved, but the modulation depth is greatly reduced. As shown in Fig. 2e,  $\Delta m$  is now ~18% at  $V_d=+3$  V as opposed to ~67% when the Stokes flow is included. This result reveals the important role of the fluid transport in enhancing the ionic current gating efficiency, primarily through reducing the ionic current in the asymmetric bias conditions.

**3.2 Fluid Transport:** Besides the ionic response, the fluidic transport in the nanopore device is also influenced by the field-effect gating. The steady-state solvent flow patterns are given in Fig. 3 for different biases ranging from symmetric to asymmetric conditions. The presence of fluid vortex flow is evident. Similar fluid vortices originating from induced electro-osmotic flow have been shown for nanochannels with charged walls [17,21]. For the voltage-gated nanopore devices in this study, the formation of vortices is found to strongly associate with the biasing symmetry. Under the symmetric biasing ( $V_d = +2$  V,  $V_g = +1$  V), a symmetric vortex pair is formed in the pore (Fig. 3a). This is a direct result of the anti-symmetric charge imbalance at the gate surface, which is further discussed later in Fig. 5a. Our results show that cations and anions drive equal amounts of fluid flow from the top and bottom pore openings, respectively. While both cation and anion fluxes go through the pore in opposite directions, the induced fluid flow cannot cross the middle plane of the nanopore. The overall result is

the formation of this symmetric vortex pair. As the bias condition becomes more asymmetric ( $V_d = +2$  V,  $V_g < 1$  V), the gate surface is modulated toward one charge polarity. The accumulated counter-ions (cations in this case) lead to the domination of the corresponding EOF component, which flows through the pore in one direction (Fig. 3b, c, d). During such a process, the co-ion driven vortex at the bottom diminishes quickly, while the counter-ion driven vortex at the top reduces slowly until the highly asymmetric bias condition is reached.

**3.3 Insights into the De-screening:** To provide additional insights on this extended field-effect gating phenomenon, we examine two specific cases for the nominal, 50 nm radius device in 1 mM KCl under symmetric ( $V_d = +2$  V,  $V_g = +1$  V) and asymmetric ( $V_d = +2$  V,  $V_g = 0$  V) bias conditions. The simulated electrostatic potential profiles are plotted for both cases in Fig. 4a & b, respectively. We observe that in contrast to the symmetric case, where the vertical potential drop occurs across the entire pore, most of the potential in the asymmetric case drops in the top portion of the pore.

In Fig. 4c, we exclusively show the electrostatic potential change induced by the gate modulation. This potential profile is obtained by subtracting the potential field of the asymmetric case from that of the symmetric case. It is clearly observed that the gate-induced potential change decays very slowly and reaches the central region of the nanopore, located 50 nm away. This is a strong indication of the long-range impact of the electrostatic control by the gate electrode, which is no longer limited by the Debye screening length. Such de-screening is distinctively different from the complete screening under equilibrium conditions. For comparison purposes, the potential profile of an equilibrium condition case is given in Fig. 4d. In that case, the field-effect gating is completely screened by the counter-ions at the gate surface, as described by the GCS model.

To quantify the de-screening, we examine the potential change at the center point ( $\Delta\psi_c$ ) induced by a modulation voltage of 1 V at the gate. The dependence of  $\Delta\psi_c$  on  $V_d$  is shown in Fig. 4e for different pore sizes and ionic strengths that correspond to the cases in Fig. 2a, b, & c. It can be seen that, under equilibrium condition ( $V_d = 0$ ),  $\Delta\psi_c$  is negligible except for the overlapping EDL case (5 nm radius, 1 mM KCl). In general,  $\Delta\psi_c$  increases with  $V_d$ , confirming the important role of transport in the de-



screening effect. For the case of 100 mM ionic strength, appreciable increase of  $\Delta\psi_c$  is clearly observed as  $V_d$  increases beyond 0.5 V despite the fact that  $R_0 \sim 50\Lambda_D$ .

We also examined the concentration profiles of the two ion species,  $C_+$  and  $C_-$ . Their difference,  $\tilde{C}_1 \equiv C_+ - C_-$ , and sum,  $\tilde{C}_2 \equiv C_+ + C_-$ , are of particular interest, since  $\tilde{C}_1$  is proportional to the net charge density and  $\tilde{C}_2$  to the total ionic conductivity. Figure 5 gives the profiles of  $\tilde{C}_1$  and  $\tilde{C}_2$  under the symmetric and asymmetric bias conditions, respectively. For the symmetric case ( $V_d = +2$  V,  $V_g = +1$  V), a moderate charge polarization with anti-symmetric profile is observed at the gate surface (Fig. 5a). As mentioned previously, such an anti-symmetry is the underlying cause of the vortex pair formation in the flow pattern shown in Fig. 3a. For the asymmetric case ( $V_d = +2$  V,  $V_g = 0$  V), the gate bias is grounded, thereby inducing significant cation accumulation (Fig. 5b). We observe that the magnitude of the cation accumulation is much lower than that of the equilibrium situation shown in Fig. S4 of the Supporting Information. This is consistent with the de-screening of the gate potential as shown in Fig. 4c.

CP is a complex of transport effects related to the formation of concentration gradients of ionic species adjacent to a charge-selective interface upon the passage of an electrical current [16]. In Fig. 5c & d, CP is observed in the profiles of  $\tilde{C}_2$ , which deviates from its bulk value of 2 mM along the vertical direction. Such an effect is moderate for the symmetric case (Fig. 5c) and significant for the asymmetric case (Fig. 5d). The observed CP effect is directly related to the extended field-effect gating. Taking the asymmetric case for example, the vertical electric field is strong in the top portion and weak in the bottom portion of the pore (Fig. 4b). The ion concentration is therefore depleted in the top portion and enriched in the bottom portion to maintain the ion flux continuity.

We note that there are dual interpretations of the observed de-screening effect from complementary perspectives. One is from the perspective of the deformed “ionic atmosphere” [23,24,25]: the counter-ion screening layer is suppressed due to strong transport along the gate surface; consequently, the channel electrostatics is modulated by the extended gating to form the high- and low-field portions,

which leads to CP to satisfy flux continuity. The other interpretation starts from the perspective of the CP theory [16]: the gated surface results in charge selectivity and flux imbalance, which lead to CP. The CP causes the formation of high and low field portions along the channel, again due to flux continuity. The channel electrostatics is therefore modulated in such a way to follow the gating potential, i.e. the gating is extended into the channel.

**3.4 Understanding Modulation Characteristics:** Based on the above observations, the gate modulation characteristics in Fig. 2a can be understood by considering the ionic transport in two portions of the nanopore: the quasi-electro-neutral central region and the charged surface EDL region [16]. The ionic transport is unipolar in the EDL region, where the transport of one ion species is dominant. In contrast, the ionic transport is ambipolar in the central region, where the concentrations of the two ion species are approximately equal. The EDL conductance increases due to enhanced accumulation of counter-ions as the gate surface is more charge polarized. This effect contributes to the slight current increase observed at extremely asymmetric biases in Fig. 2a. It dominates in the  $I_d$ - $V_g$  characteristics in small nanopores with overlapping EDLs (Fig. 2b).

The current suppression around the symmetric bias conditions occurs for nanopores with non-overlapping EDLs (Fig. 2a & c). We believe such current suppression originates from ambipolar transport in the central region of the pore. This is supported by the plots in Fig. 6a, where the electrostatic potential, ion concentrations, and the chemical potentials of the two ion species,  $\phi_{\pm} \equiv \pm \frac{kT}{q} \ln(C_{\pm}) + \psi$ , are plotted along the central axis for the asymmetric bias case ( $V_d = +2$  V,  $V_g = 0$  V). The extended field-effect gating is clearly observed in the electrostatic potential curve. We also observe that the drift process dominates over the diffusion process as indicated by the small difference between electrostatic and chemical potentials. The difference between the cation and anion concentrations is only appreciable at locations where the electric field strength changes rapidly, as dictated by the Poisson equation. At most locations, the two ion concentrations are approximately equal, suggesting the ambipolar nature of the transport. The correspondence between the ion depletion (enrichment) and the

high (low) field strength is observed, satisfying ionic flux continuity. The formation of such enrichment and depletion regions is known to limit the over-all ionic conductance [16,19].

The important role of the coupled fluid transport in the ionic current modulation is further examined in Fig. 6b, where the electrostatic potential ( $\psi$ ) and the total ion concentration ( $\tilde{C}_2$ ) along the central axis are shown for two simulations: the full model including the Stokes flow and the PNP-only model. For the asymmetric biasing condition, the ionic current is further suppressed by the EOF pattern shown in Fig. 3c in two ways. Firstly, the EOF carries away the counter-ions accumulated at the gate surface, leading to enhanced field-effect gating. Secondly, the EOF carries both ion species in the pore toward the bottom reservoir. This decreases the ion concentration in the bottom, low-field portion of the pore and causes additional current reduction.

#### 4. CONCLUSIONS:

In summary, we have numerically investigated the ionic and fluidic transport characteristics in field-effect gated nanopores with non-overlapping EDLs. It is revealed that the field effect is dramatically extended far beyond the Debye screening length and results in efficient modulation of both ionic and fluidic transport. The field effect is significant even in nanopores with radii  $\sim 50\Lambda_D$ . We attribute such an extended field effect to the de-screening of counter-ions at the gate surfaces in the presence of strong transport processes. The enhanced gating leads to highly nonlinear device I-V characteristics, which are found to strongly associate with concentration polarization and induced electro-osmotic flow. We believe that the revealed de-screening behavior is a general effect manifested under sufficiently high electric fields, which may be practically reached using nano-devices. The resultant long-range electrostatic interaction could form the basis for direct manipulation of charged species in nano-fluidic systems.

**ACKNOWLEDGMENTS:** We appreciate discussions with R.T. Howe, J. Sauer, and J. Snapp on the de-screening mechanism, J. Santiago and T. Zangle on concentration polarization, and C. Rafferty on numerical methods.

## References:

x

- [1] J. J. Kasianowicz, E. Brandin, D. Branton, and D. W. Deamer, "Characterization of individual polynucleotide molecules using a membrane channel," *Proc. Natl. Acad. Sci.*, vol. 93, no. 24, pp. 13770-13773, 1996.
- [2] S. Howorka, S. Cheley, and H. Bayley, "Sequence-specific detection of individual DNA strands using engineered nanopores," *Nature Biotechnology*, vol. 19, no. 7, pp. 636-639, 2001.
- [3] C. Dekker, "Solid-state nanopores," *Nature Nanotechnology*, vol. 2, pp. 209-215, 2007.
- [4] D. Branton, "The potential and challenges of nanopore sequencing," *Nature Biotechnology*, vol. 26, pp. 1146-1153, 2008.
- [5] V. Tarbad-Cossa et al., "Single-molecule bonds characterized by solid-state nanopore force spectroscopy," *ACS Nano*, vol. 3, pp. 3009-3014, 2009.
- [6] S. M. Sze and K. K. Ng, *Physics of Semiconductor Devices*, 3th ed. Hoboken, NJ: Wiley, 2007.
- [7] B. M. Schasfoort, S. Schlautmann, J. Hendrikse, and A. van den Berg, "Field-effect flow control for microfabricated fluidic networks," *Science*, vol. 286, pp. 942-945, 1999.
- [8] R. Karnik et al., "Electrostatic Control of Ions and Molecules in Nanofluidic Transistors," *Nano Letters*, vol. 5, no. 5, pp. 943-948, 2005.
- [9] H. Daiguji, Y. Oka, and K. Shirono, "Nanofluidic diode and bipolar transistor," *Nano Letters*, vol. 5, pp. 2274-2280, 2005.
- [10] M. E. Gracheva, D. V. Melnikov, and J. P. Leburton, "Multilayered semiconductor membranes for nanopore ionic conductance modulation," *ACS Nano*, vol. 2, pp. 2349-2355, 2008.
- [11] E. B. Kalman, I. Vlassiuk, and Z. S. Siwy, "Nanofluidic bipolar transistors," *Advanced Materials*, vol. 20, pp. 293-297, 2008.
- [12] S. W. Nam, M. J. Rooks, K.-B. Kim, and S. M. Rossnagel, "Ionic field effect transistors with sub-10 nm multiple nanopores," *Nano Letters*, vol. 9, no. 5, pp. 2044-2048, 2009.
- [13] R. Fan, S. Huh, R. Yan, J. Arnold, and P. Yang, "Gated proton transport in aligned mesoporous silica films," *Nature Materials*, vol. 7, pp. 303-307, 2008.
- [14] K. Y. Chun, S. Mafe, P. Ramirez, and P. Stroeve, "Protein transport through gold-coated, charged nanopores: Effects of applied voltage," *Chemical Physics Letters*, vol. 418, pp. 561-564, 2006.
- [15] Q. Pu, J. Yun, H. Temkin, and S. Liu, "Ion-enrichment and ion-depletion effect of nanochannel structures," *Nano Letters*, vol. 4, pp. 1099-1103, 2004.
- [16] A. Holtzel and U. Tallarek, "Ionic conductance of nanopores in microscale analysis systems: Where microfluidics meets nanofluidics," *J. Sep. Sci.*, vol. 30, pp. 1398-1419, 2007.
- [17] S. J. Kim, Y.-C. Wang, J. H. Lee, H. Jang, and J. Han, "Concentration polarization and nonlinear

- electrokinetic flow near a nanofluidic channel," *Physical Review Letters*, vol. 99, p. 044501, 2007.
- [18] I. Vlassiounk, S. Smirnov, and Z. Siwy, "Ionic Selectivity of Single Nanochannels," *Nano Letters*, vol. 8, no. 7, pp. 1978-1985, 2008.
- [19] A. Mani, T. A. Zangle, and J. G. Santiago, "On the propagation of concentration polarization from microchannel-nanochannel interfaces part I: analytical model and characteristic analysis," *Langmuir*, vol. 25, pp. 3898-3908, 2009.
- [20] T. A. Zangle, A. Mani, and J. G. Santiago, "On the propagation of concentration polarization from microchannel-nanochannel interfaces part II: numerical and experimental study," *Langmuir*, vol. 25, pp. 3909-3916, 2009.
- [21] G. Yossifon and H.-C. Chang, "Selection of nonequilibrium overlimiting currents: universal depletion layer formation dynamics and vortex instability," *Phys. Rev. Lett.*, vol. 101, p. 254501, 2008.
- [22] A. J. Bard and L. R. Faulkner, *Electrochemical Methods: Fundamentals and Applications*, 2th ed.: John Wiley & Sons Inc., 2001.
- [23] L. Onsager and R. M. Fuoss, "Irreversible processes in electrolytes. Diffusion, conductance, and viscous flow in arbitrary mixtures of strong electrolytes," *J. Phys. Chem.*, vol. 36, pp. 2689-2778, 1932.
- [24] L. Onsager and S. K. Kim, "Wien effect in simple strong electrolytes," *Journal of Physical Chemistry*, vol. 61, pp. 198-215, 1957.
- [25] L. Onsager and S. K. Kim, "The relaxation effects in mixed strong electrolytes," *J. Phys. Chem.*, vol. 61, pp. 215-229, 1957.
- [26] M.-S. Chen, "Wien effect in mixed strong electrolytes," *J. Chem. Phys.*, vol. 68, pp. 5442-5447, 1978.
- [27] Y. Liu, J. Sauer, and R. W. Dutton, "Effect of electro-diffusion current flow on electrostatic screening in aqueous pores," *Journal of Applied Physics*, vol. 103, p. 084701, 2008.
- [28] Y. Liu, K. Lilja, C. Heitzinger, and R. W. Dutton, "Overcoming the screening-induced performance limits of nanowire biosensors: a simulation study on the effect of electro-diffusion flow," in *IEDM Tech. Dig.*, San Francisco, 2008, pp. 491-4.
- [29] Y. Liu and R. W. Dutton, "Effects of charge screening and surface properties on signal transduction in field effect nanowire biosensors," *J. App. Phys.*, vol. 106, p. 014701, 2009.
- [30] L. Bousse, "Single electrode potentials related to flat-band voltage measurements on EOS and MOS structures," *J. Chem. Phys.*, vol. 76, no. 10, pp. 5128-5133, 1982.
- [31] J. Happel and H. Brenner, *Low Reynolds Number Hydrodynamics: With Special Applications to Particulate Media*. Boston: Springer, 1983.
- [32] R. W. Dutton and Z. Yu, *Technology CAD*. Norwell, MA: Kluwer, 1993.

- [33] J. H. Ferziger and M. Peric, *Computational Methods for Fluid Dynamics*, 3th ed.: Springer, 2002.
- [34] M. Wanunu and A. Meller, "Chemically modified solid-state nanopores," *Nano Letters*, vol. 7, pp. 1580-1585, 2007.

x

### List of Figure Captions:

Fig. 1: Schematic plot of gated nanopore device structure with cylindrical symmetry (not to scale). Unless otherwise specified, the nominal device parameters include: pore radius  $R_0=50$  nm; top and bottom oxide thickness 100 nm each; gate electrode thickness 100 nm; gate oxide thickness  $t_1 = 2$  nm; reservoir size 1  $\mu\text{m}$  in both width and thickness; and surface charge density  $\sigma_s = 0$ .

Fig. 2: (a)-(d)  $I_d$ - $V_g$  characteristics for (a) the nominal 50 nm radius device in 1 mM KCl; (b) a smaller, 5 nm radius nanopore device in 1 mM KCl; (c) the nominal 50 nm radius device in 100 mM KCl; and (d) the nominal device in 1 mM KCl but only with the PNP model, i.e. no fluid transport. The  $V_d$  bias of the  $I_d$ - $V_g$  curves ranges from 0 V to 3 V at a step of 0.2 V. The dark dashed line in each figure corresponds to the ionic current at symmetric bias conditions,  $I_d(V_d, V_g=\frac{1}{2} V_d)$ . (e) Current modulation depth,  $\Delta m$ , as functions of the drain bias,  $V_d$ , for the cases of (a), (c) and (d), respectively.

Fig. 3: Vector plots of fluid flow velocities for a constant  $V_d$  of 2 V and varying  $V_g$  biases from symmetric to more asymmetric: (a)  $V_g = +1$  V; (b)  $V_g = +0.5$  V; (c)  $V_g = 0$  V; (d)  $V_g = -0.5$  V. Only the portion near the nanopore is shown. The velocity scale references are given for both radial and vertical directions in each figure. The dashed, thick arrows are for visual guide only.

Fig. 4: (a)-(d) Electrostatic potential (unit: V) of the nominal device for (a) symmetric biasing where  $V_g = +1$  V and  $V_d = +2$  V; (b) asymmetric biasing where  $V_g = 0$  V and  $V_d = +2$  V; (c) potential difference between the symmetric and asymmetric cases; (d) a comparative, equilibrium case where  $V_g = +1$  V and  $V_d = 0$  V. Only the portion near the nanopore is shown. (e) Under a gate modulation of 1 V, the induced potential difference at the center point,  $\Delta\psi_c$ , as functions of  $V_d$  for three cases corresponding to Fig. 2a, b & c, respectively.

Fig. 5: The difference ( $\tilde{C}_1 \equiv C_+ - C_-$ ) and sum ( $\tilde{C}_2 \equiv C_+ + C_-$ ) of ion concentrations (unit: mM) for symmetric ( $V_d = 2$  V,  $V_g = 1$  V) and asymmetric ( $V_d = 2$  V,  $V_g = 0$  V) bias conditions: (a)  $\tilde{C}_1$  at symmetric biasing; (b)  $\tilde{C}_1$  at asymmetric biasing; (c)  $\tilde{C}_2$  at symmetric biasing; and (d)  $\tilde{C}_2$  at asymmetric biasing. Only the portion near the nanopore is shown.

Fig. 6: (a) Electrostatic potential ( $\psi$ ), chemical potentials ( $\phi_+$  and  $\phi_-$ ), and ion concentrations ( $C_+$  and  $C_-$ ) along the central axis; (b) profiles of electrostatic potential ( $\psi$ ) and the sum of ion concentrations ( $\tilde{C}_2 \equiv C_+ + C_-$ ) along the central axis from the full model and the PNP-only model, respectively. The top and bottom edges of the pore are marked by the vertical lines. For both figures, the nominal device is simulated with 1 mM KCl under the asymmetric biasing condition ( $V_g = 0$  V,  $V_d = 2$  V).



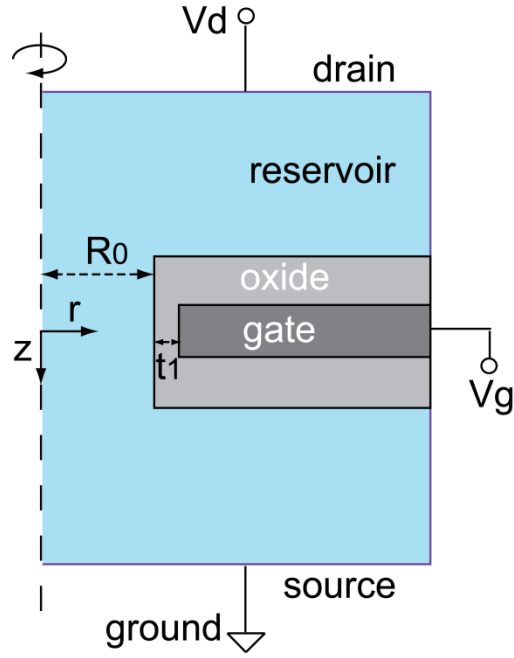


Fig. 1: Schematic plot of gated nanopore device structure with cylindrical symmetry (not to scale). Unless otherwise specified, the nominal device parameters include: pore radius  $R_0=50$  nm; top and bottom oxide thickness 100 nm each; gate electrode thickness 100 nm; gate oxide thickness  $t_1 = 2$  nm; reservoir size  $1\text{ }\mu\text{m}$  in both width and thickness; and surface charge density  $\sigma_s = 0$ .

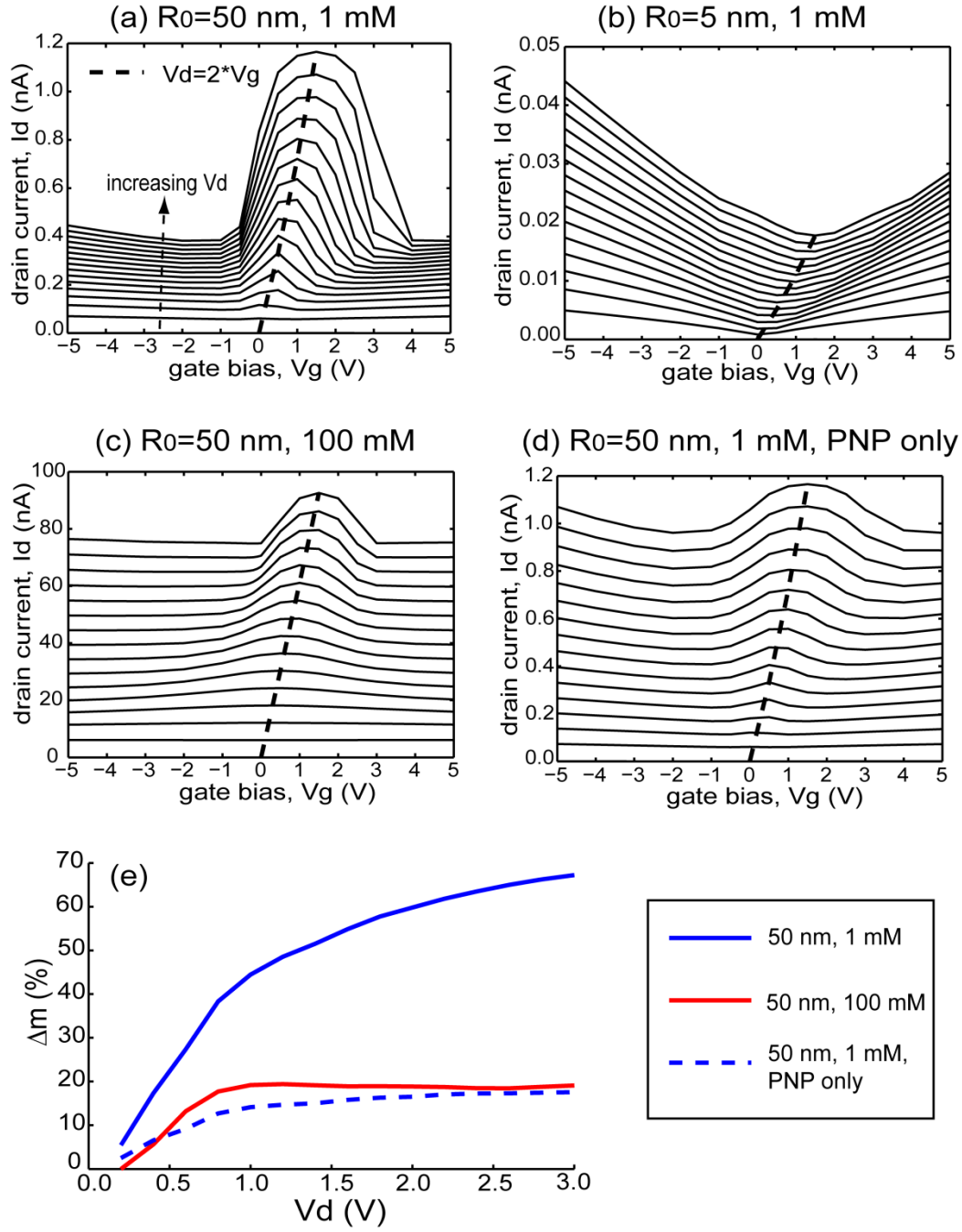


Fig. 2: (a)-(d)  $I_d$ - $V_g$  characteristics for (a) the nominal 50 nm radius device in 1 mM KCl; (b) a smaller, 5 nm radius nanopore device in 1 mM KCl; (c) the nominal 50 nm radius device in 100 mM KCl; and (d) the nominal device in 1 mM KCl but only with the PNP model, i.e. no fluid transport. The  $V_d$  bias of the  $I_d$ - $V_g$  curves ranges from 0 V to 3 V at a step of 0.2 V. The dark dashed line in each figure corresponds to the ionic current at symmetric bias conditions,  $I_d(V_d, V_g=\frac{1}{2} V_d)$ . (e) Current modulation depth,  $\Delta m$ , as functions of the drain bias,  $V_d$ , for the cases of (a), (c) and (d), respectively.

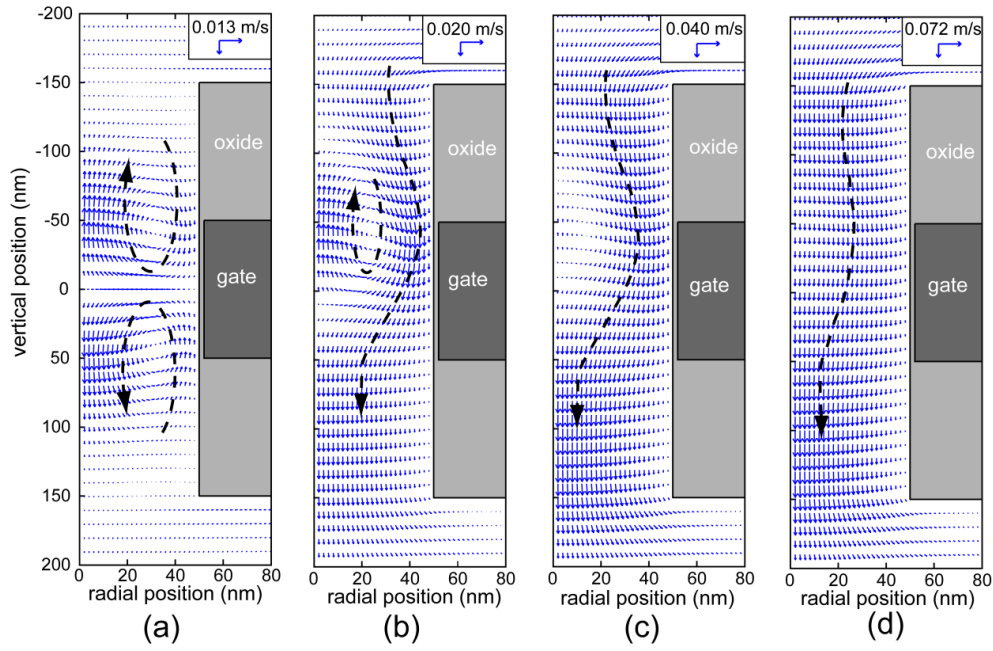


Fig. 3: Vector plots of fluid flow velocities for a constant  $V_d$  of 2 V and varying  $V_g$  biases from symmetric to more asymmetric: (a)  $V_g = +1$  V; (b)  $V_g = +0.5$  V; (c)  $V_g = 0$  V; (d)  $V_g = -0.5$  V. Only the portion near the nanopore is shown. The velocity scale references are given for both radial and vertical directions in each figure. The dashed, thick arrows are for visual guide only.

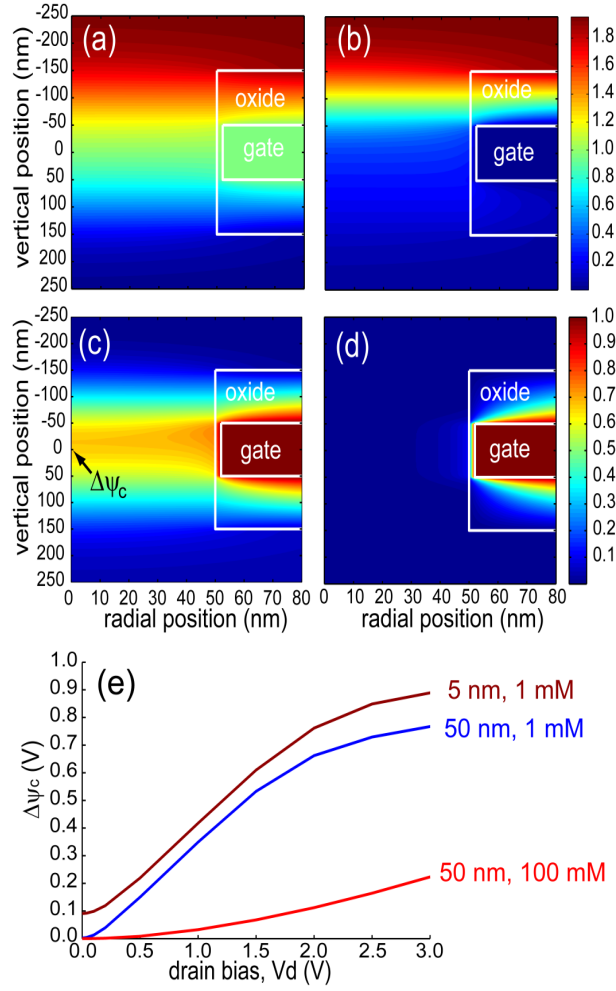


Fig. 4: (a)-(d) Electrostatic potential (unit: V) of the nominal device for (a) symmetric biasing where  $V_g = +1$  V and  $V_d = +2$  V; (b) asymmetric biasing where  $V_g = 0$  V and  $V_d = +2$  V; (c) potential difference between the symmetric and asymmetric cases; (d) a comparative, equilibrium case where  $V_g = +1$  V and  $V_d = 0$  V. Only the portion near the nanopore is shown. (e) Under a gate modulation of 1 V, the induced potential difference at the center point,  $\Delta\psi_c$ , as functions of  $V_d$  for three cases corresponding to Fig. 2a, b & c, respectively.

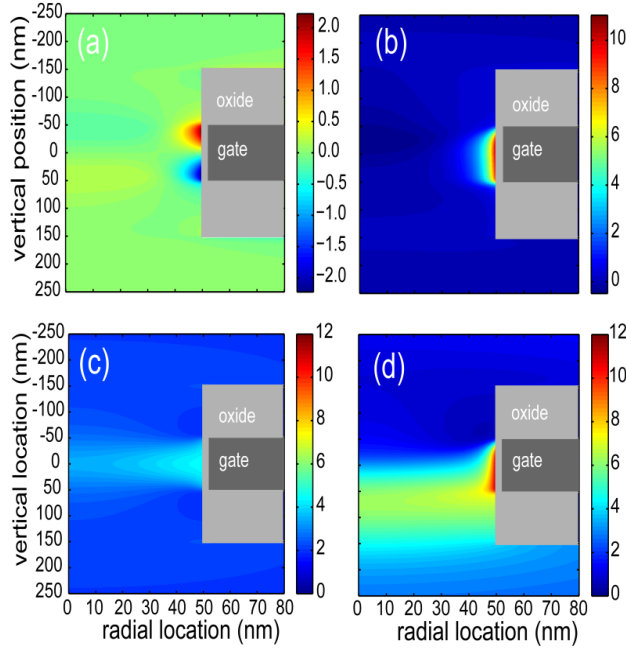


Fig. 5: The difference ( $\tilde{C}_1 \equiv C_+ - C_-$ ) and sum ( $\tilde{C}_2 \equiv C_+ + C_-$ ) of ion concentrations (unit: mM) for symmetric ( $V_d = 2$  V,  $V_g = 1$  V) and asymmetric ( $V_d = 2$  V,  $V_g = 0$  V) bias conditions: (a)  $\tilde{C}_1$  at symmetric biasing; (b)  $\tilde{C}_1$  at asymmetric biasing; (c)  $\tilde{C}_2$  at symmetric biasing; and (d)  $\tilde{C}_2$  at asymmetric biasing. Only the portion near the nanopore is shown.

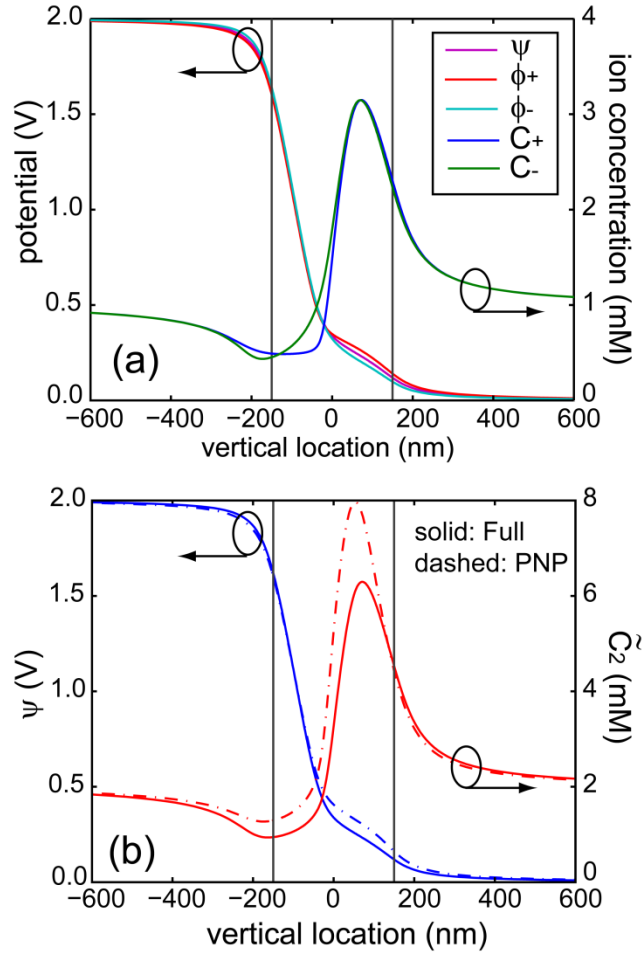


Fig. 6: (a) Electrostatic potential ( $\psi$ ), chemical potentials ( $\phi_+$  and  $\phi_-$ ), and ion concentrations ( $C_+$  and  $C_-$ ) along the central axis; (b) profiles of electrostatic potential ( $\psi$ ) and the sum of ion concentrations ( $\tilde{C}_2 \equiv C_+ + C_-$ ) along the central axis from the full model and the PNP-only model, respectively. The top and bottom edges of the pore are marked by the vertical lines. For both figures, the nominal device is simulated with 1 mM KCl under the asymmetric biasing condition ( $V_g = 0$  V,  $V_d = 2$  V).

# Supporting Information for “Extended field-effect gating on ionic and fluidic transport in nanopores”

*Yang Liu<sup>\*1</sup>, David E. Huber<sup>2</sup>, Vincent Tabard-Cossa<sup>2</sup>, and Robert W. Dutton<sup>1</sup>*

<sup>1</sup>Center for Integrated Systems, Stanford University, CA 94305

<sup>2</sup>Stanford Genome Technology Center, Palo Alto, CA 94304

E-mail: [yangliu@gloworm.stanford.edu](mailto:yangliu@gloworm.stanford.edu), phone: 1-650-723-9796, fax: 1-650-725-7731

**Numerical model validation:** we test the validity of our numerical model through comparisons with published results and analytical models. In the first test case, we solve the PNP equations for a nano-channel model system that exactly follows that in Fig. 1 of Ref. [18]. Two reservoirs (1  $\mu\text{m}$  radius X 1  $\mu\text{m}$  height) are connected by a cylindrical nano-channel. The channel radius is 4 nm and length 128 nm. The bulk KCl concentration is 0.1 M, the channel surface charge density  $-0.5 \text{ q/nm}^2$ , and the applied bias 0 V. The simulated cation and anion concentrations and longitudinal electrical field are plotted in Fig. S1, which reproduce the results presented in Fig. 1A of Ref. [18].

The second test case is the electro-osmotic flow (EOF) in a long, cylindrical nano-channel. For cylindrical symmetry, there are no general analytical

solutions for the electrostatic potential,  $\psi$ , and the longitudinal flow velocity,  $u$ . Nevertheless, it is

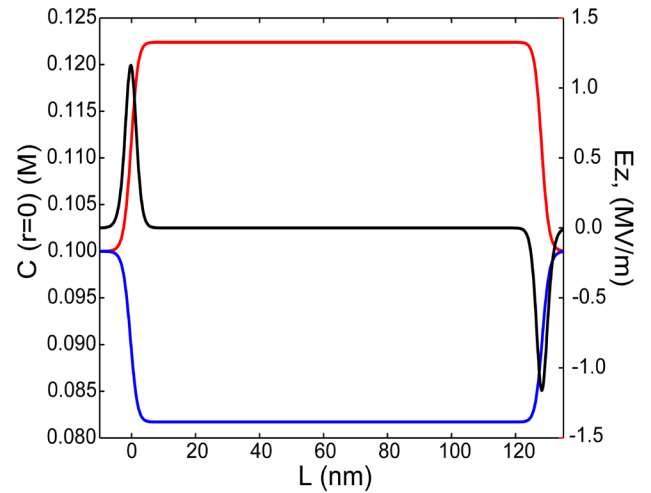


Fig. S1: longitudinal profiles of cation (Red) and anion (Blue) concentrations and electric field (Black) simulated using the PNP solver for a nano-channel test case that exactly follows Fig. 1 of Ref. [18].

known that, in the limit of long channel, low longitudinal electric field and fully developed EOF process, an analytical relation applies between  $\psi$  and  $u$  as follows Ref [8] & [18]:

$$u(r) = \frac{\varepsilon_w E_z}{\gamma} [\psi(r) - \psi(R_0)],$$

Eq. S1

where  $r$  is the radial position,  $R_0$  the channel radius,  $\varepsilon_w$  the solution permittivity,  $\gamma$  the solvent viscosity, and  $E_z$  the longitudinal electrical field. We simulate the coupled PNP and Stokes equations for a nano-channel with radius of 100 nm, length of 2  $\mu\text{m}$ , surface charge density of -0.2 q/nm<sup>2</sup>,  $\varepsilon_w$  of  $80\varepsilon_0$ ,  $\gamma$  of 0.001 Ns/m<sup>2</sup>, and applied bias of 0.1 V. The simulated radial profile of solvent velocity is given in Fig. S2. As a comparison, we also plot the velocity profile obtained from Eq. S1 using simulated  $\psi(r)$ . The good agreement between the two profiles validates our EOF model.

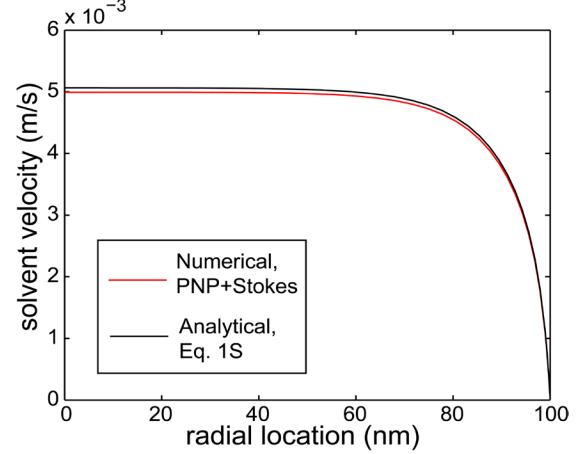


Fig. S2: Radial profiles of the solvent velocity for a long nano-channel test case. Results from both the fully numerical simulation and the analytical model of Eq. (S1) are shown.

**Effect of reservoir size:** It is important to examine whether the CP effect propagates and whether the finite reservoir size artificially suppresses any CP effect (Ref. [20]). For that purpose, a comparative simulation study is conducted for the nominal device with two different reservoir sizes, 1  $\mu\text{m}$  (nominal) and 10  $\mu\text{m}$ , respectively. The simulated  $I_d$ - $V_g$  characteristics for both devices are given in Fig. S3. It is confirmed that the reservoir size does not affect the fidelity of our simulation results.

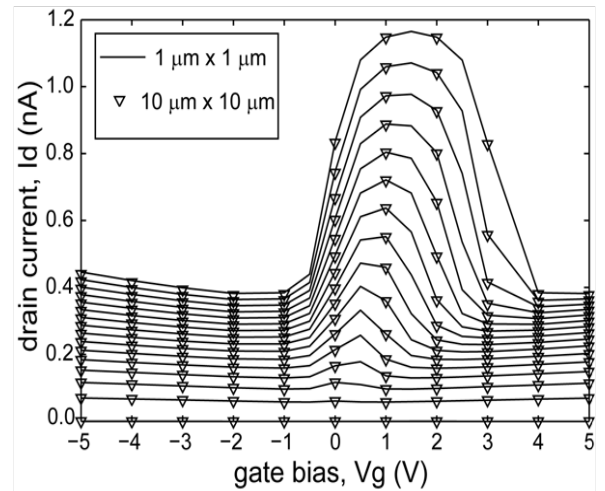


Fig. S3: simulated  $I_d$ - $V_g$  characteristics for the nominal device with two different reservoir sizes, 1  $\mu\text{m}$  and 10  $\mu\text{m}$ , respectively. The  $V_d$  ranges from 0 V to 3 V at a step of 0.2 V.



**Profile of  $\tilde{C}_1$  under equilibrium:** we study an equilibrium bias condition for comparison purposes.

The simulated ion concentration difference,  $\tilde{C}_1 \equiv C_+ - C_-$ , is plotted in Fig. S4. Both the source and the drain are grounded, i.e. under equilibrium condition, and the gate bias is -1 V. It is observed in Fig. S4 that cations accumulate at the gate surface with a maximum concentration greater than 60 mM. This peak value is much higher than that of the de-screening case ( $\sim 10$  mM) as shown in Fig. 5b.

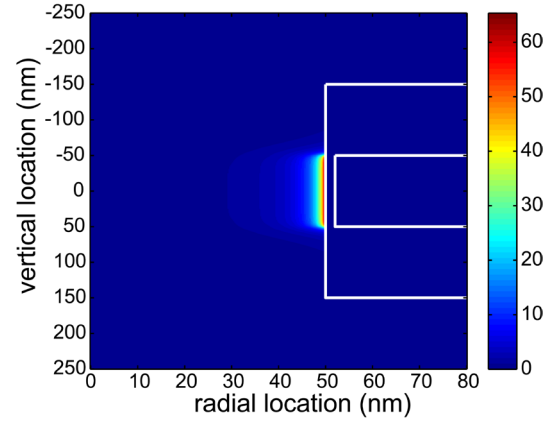


Figure S4:  $\tilde{C}_1$  (unit: mM) for the nominal device under an equilibrium condition ( $V_d = 0$  V,  $V_g = -1$  V.)

**Effect of surface charge:** Both the sign and magnitude of surface charges can be controlled by pH or surface chemistry (Ref. [33]), which can be used to engineer the transport characteristics (Ref. [18]). For the devices under study, the presence of surface charge breaks the symmetry between the two charge polarities and substantially complicates the overall transport

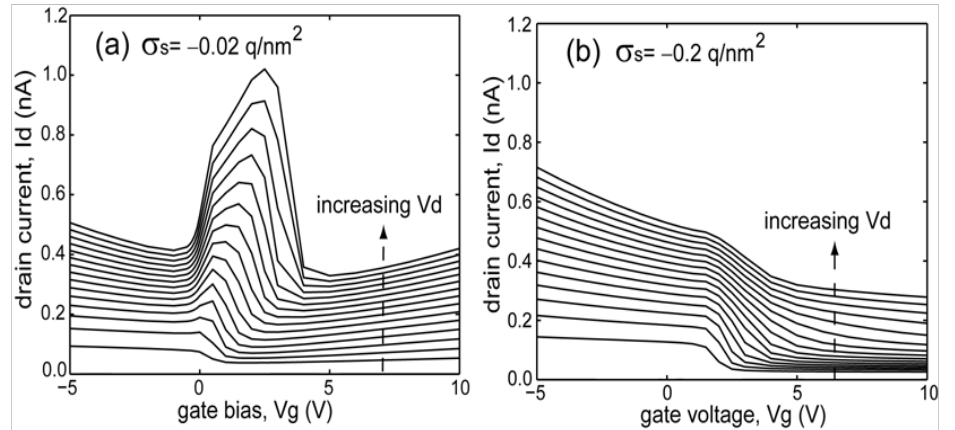


Fig. S5: Simulated  $I_d$ - $V_g$  characteristics for the nominal, 50 nm radius device with finite nanopore surface charge density (a)  $-0.02$  q/nm<sup>2</sup>, and (b)  $-0.2$  q/nm<sup>2</sup>, respectively. The range of  $V_d$ 's is the same as that in Fig. 2.

process. In Fig. S5, the simulated  $I_d$ - $V_g$  characteristics are shown for the nominal device with nanopore surface charge densities of  $-0.02$  q/nm<sup>2</sup> and  $-0.2$  q/nm<sup>2</sup>, respectively. In comparison with Fig. 2a, the basic modulation characteristics are preserved for the case of lower surface charge density (Fig. S5a). The  $I_d$ - $V_g$  curves shift to the positive  $V_g$  side, since the gate bias needs to overcome the negative surface potential that is induced by the surface charges. An additional modulation effect is observed, where the

current is enhanced at the negative  $V_g$  side. This effect becomes dominant for the case of higher surface charge density, where one-sided “shoulders” instead of the symmetric peaks are observed (Fig. S5b). The current enhancement at the negative  $V_g$  side is believed to result from the dominant surface EDL conductance in the presence of significant negative surface charges. At more negative  $V_g$ 's, the gate surface is polarized to cation accumulation, which connects a highly conductive path of cations in the surface EDL region. On the other hand, when the gate surface is polarized to cation depletion at more positive  $V_g$ 's, the surface EDL conducting path is switched off. In this case, the major conducting path is through the central region.